Confidence-Based Buffer for Strategic Deconfliction with Probabilistic Operational Intent

José Ignacio de Alvear Cárdenas*†
San José State University, Moffett Field, CA 94035, USA

Priyank Pradeep‡
Universities Space Research Association, Moffett Field, CA 94035, USA

Min Xue§ and Seungman Lee¶
NASA Ames Research Center, Moffett Field, CA 94035, USA

Vincent H. Kuo‖
Metis Technology Solutions, Moffett Field, CA 94035, USA

This paper presents a methodology to expand the 95% confidence level of the elliptical geometry given by Unmanned Aircraft System (UAS) operators planning to fly Beyond Visual Line of Sight (BVLOS) to any confidence level before being fed to the strategic deconfliction (SD) module, effectively increasing the separation buffer between Operational Intents (OIs). To assess the performance of this approach, it is integrated within an adaptation of the Rolling Horizon with K-Position Search volume-based strategic deconfliction approach, previously developed at NASA Ames, preventing the 4D overlapping of OIs shaped by ellipses instead of traditional blocks. Safety and efficiency metrics are evaluated through the deconfliction of four simulated package delivery route network structures across the San Francisco Metropolitan Area with increasing numbers of crossing waypoints (network complexity). Safety assessment entails the in-house creation of a metric to quantify collision occurrences per flight hour based on the frequency at which the probabilistic operational volume segments are sampled, whereas efficiency is measured using ground delay. Results indicate that the largest buffer growth occurs when increasing the confidence level beyond 99.9% and demonstrate the negative impact of network complexity on both metrics, regardless of the OI geometry. Further, the ellipse-based SD adaptation more accurately estimates temporal separation at crossings, allowing deconflicted vehicles to be closer together. It is concluded that the proposed methodology enables the desired confidence level to serve as an effective controller of buffer size.

I. Nomenclature

a, b	=	ellipse main semi-axes lengths
C	=	set of unordered flight pairs simultaneously in the air
c, m	=	line intersection point with the y-axis and line slope
d	=	Mahalanobis distance
e, f	=	ellipse and flight
$\mathcal{F}$	=	set of all flights of a scenario in chronological order
$\boldsymbol{I}, \boldsymbol{Q}$	=	intersection and arbitrary points
k	=	degrees of freedom of the chi-square distribution
$\boldsymbol{L}$	=	lower triangular matrix of the Cholesky decomposition of a covariance matrix

*Aerospace Research Engineer, Human Systems Integration Division, NASA Ames Research Center, AIAA Member.
†Corresponding author: jose.dealvearcardenas@sjsu.edu
‡Senior Aerospace Engineer, Universities Space Research Association, NASA Ames Research Center, AIAA Senior Member.
§Aerospace Research Engineer, Aviation Systems Division, NASA Ames Research Center, AIAA Senior Member.
¶Senior Aerospace Engineer, Aviation Systems Division, NASA Ames Research Center, AIAA Senior Member.
‖Principal Project Systems Engineer, Metis Technology Solutions, NASA Ames Research Center, AIAA Member.

L = overlapping ellipse distances
M, N = confidence level
$N_{\alpha i}$ = number of samples drawn from elliptical operational segment i of flight α
n_f = number of flights in scenario
$\boldsymbol{P}^*$, θ^* = point on ellipse closest to a circle and its ellipse parametric equation angle
$\boldsymbol{R}$, τ = rotation matrix and angle
r = number of routes in scenario
t = time
T = probability sampling rate
V_c = cruise ground speed
$\boldsymbol{Z}$ = standard normal distribution features
α, β = flight names
γ = gradient descent learning rate
η = angle between the ownship's line and the intruder's flight path
$\boldsymbol{\lambda}$ = covariance matrix eigenvalues
$\boldsymbol{\mu}$, $\boldsymbol{\Sigma}$, $\boldsymbol{X}$ = multivariate normal distribution mean, covariance matrix and sample
ξ = percentage of ellipse temporal overlap
σ = traffic density of a single route
ϕ, $\boldsymbol{v}$ = azimuth angle and flight path vector
ω = decision variable

II. Introduction

According to the Operational Intent (OI) requirement OPIN0010 from the ASTM 2021 document titled "Standard Specification for Unmanned Aircraft System (UAS) Traffic Management (UTM) UAS Service Supplier (USS) Interoperability" [1], it is expected that operational intents are constructed such that "the UA's actual position is inside an operational intent in the Activated state at least *OiMinConformance* percent of total flight time", where *OiMinConformance* is 95%. As a result, strategic deconfliction (SD) approaches which assume guaranteed safety by only avoiding overlap between OIs [2] may be underestimating the collision risk, as UAS are expected to deviate from their OI up to 5% of the time. These SD strategies consider the OI to be deterministic for safety purposes, allowing OIs to be positioned in close proximity or even tangentially to each other, despite the UAS's position being stochastic and only probabilistically certain within the OI. Hence, the safety of these approaches could be improved by adjusting the shape of the OIs to ensure they encapsulate the UAS for a higher percentage of time than the 95% provided by operators — such as 99%, for example. Other SD approaches [3, 4] understand the stochastic nature of the OI, but calculate the safety risk numerically with Monte Carlo simulations, which can be computationally expensive.

Furthermore, the operational volume segments that shape an OI have been defined as blocks by the UTM Concept of Operations (ConOps) [5], which the research community has interpreted as spatio-temporal 4D cuboids [2–4, 6–8] and sometimes refer to as Operational Volume Blocks (OVBs) [2]. However, assuming that the position of the flying vehicle follows a normal distribution $\boldsymbol{X} \sim \mathcal{N}(\boldsymbol{\mu}, \boldsymbol{\Sigma})$ [8–10], these deterministic cuboids (rectangles in 2D) are a simplification that encapsulate the probabilistic ellipsoids (ellipses in 2D) that signify a 95% confidence level. Therefore, when the vehicles operate at the same flight level, using ellipses instead of rectangles could enhance 2D deconfliction.

Hence, this research proposes a method that increases OVBs size beyond the 95% given by operators who are expected to fly Beyond Visual Line of Sight (BVLOS). Since blocks could be tangential to each other, this would enhance safety by effectively adding an additional separation safety buffer. The impact of the buffer is assessed by integrating it within an adaptation of the SD approach developed at NASA Ames called "Rolling Horizon with K-Position Search" [11] that separates the elliptical Operational Volume Segments (OVSs) instead of their standard blocks. Finally, the safety and efficiency of this new approach are evaluated across four simulated scenarios of increasing complexity, alongside an exploration of the impact of confidence level manipulation and OVB/OVS geometry on those same metrics.

The remainder of this paper is organized as follows. Section III outlines the methodology, including the technique for manipulating the elliptical geometry through confidence levels, the adapted strategic deconfliction approach, the safety and efficiency metrics, and a description of the road network structures defining the testing scenarios. Then, Section IV covers the results, highlighting the impact of the OVB/OVS geometry and the confidence level on the safety-efficiency trade-off, as well as the influence of scenario complexity on these metrics. Here, computation time is briefly discussed. Finally, Section V synthesizes the main conclusions from this analysis and discusses avenues of future research.

III. Methodology

A. Confidence-based OVB size manipulation

A confidence ellipse representing a bivariate normal distribution encircles the region in which a specified proportion of the distribution's probability mass lies, 95% in the case of those encapsulated by the OVBs provided by BVLOS operators. It is characterized by its mean $\boldsymbol{\mu}$, which marks its center, and its covariance matrix $\boldsymbol{\Sigma}$, representing the relationship between the two distribution variables. The major and the minor axes of the ellipse align with the eigenvectors of the covariance matrix, and their lengths are scaled to the standard deviations of the distributions along these axes. The rest of this section will explain how that scaling is defined given a certain level of confidence.

The samples of a normal distribution can be standardized by subtracting their mean and dividing by their standard deviation, as in Equation 1. The resulting features ($\boldsymbol{Z}$) become uncorrelated with each other with $\boldsymbol{\mu_Z} = \mathbf{0}$ and $\boldsymbol{\Sigma_Z} = \mathbf{I}$, describing a standard normal distribution. In this transformed space, points that form a circle with radius d, as given in Equation 2, define an ellipse in the original space when reversing the transformation. This can be visualised in Figure 1. The goals are to determine the distance d in the transformed space that encapsulates 95% of the samples, thereby establishing the 95% confidence contours in the original space through its elliptical representation, and understanding its relationship with the geometric properties of the ellipse.

$$\boldsymbol{Z} = \boldsymbol{\Sigma}^{-0.5}(\boldsymbol{X} - \boldsymbol{\mu}) \qquad (1)$$

$$(\boldsymbol{X} - \boldsymbol{\mu})^T \boldsymbol{\Sigma}^{-1} (\boldsymbol{X} - \boldsymbol{\mu}) = d^2;\ \boldsymbol{Z}^T \boldsymbol{Z} = d^2 \qquad (2)$$

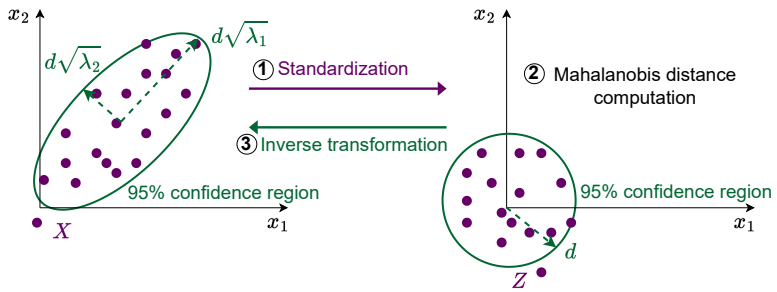

Fig. 1 Dataset standardization, Mahalanobis distance computation and confidence ellipse sizing.

The distance d is called the Mahalanobis distance and every point in the ellipse is said to have the same Mahalanobis distance to the center of the ellipse. In contrast with the Euclidean distance, which treats each variable independently, the Mahalanobis distance accounts for correlation between variables of a multivariate normal distribution when measuring how many standard deviations away a sample is from the distribution's mean. The squared Mahalanobis distance follows a chi-square distribution (χ^2_k) with k degrees of freedom, where k represents the number of dimensions (in this case, k=2 for two-dimensional ellipses). This distribution arises from the sum of squares of k independent standard normal random variables, as shown to be the case here by Equation 3. Consequently, the distance d in the transformed space containing 95% of the data points is determined using the inverse cumulative density function (ICDF) of the chi-square distribution. The ICDF is usually retrieved from statistical tables found in standard textbooks which provide critical values corresponding to specific probabilities for different degrees of freedom. For instance, at a 95% confidence level and 2 degrees of freedom, $(\chi^2_2)^{-1}(0.95) = d^2 = 5.99\ [\mathrm{m}^2] \rightarrow d = 2.45[m]$.

$$\boldsymbol{Z}^T \boldsymbol{Z} = \sum_i^k Z_i^2 = d^2 \sim \chi^2_k \qquad (3)$$

Since the covariance matrix in the transformed space is the identity matrix, when the Mahalanobis distance equals 1, the points on the circle are precisely one standard deviation away from the mean; the Mahalanobis distance measures how many standard deviations away a point is from the mean of a distribution. In the original space, the principal axes align with the eigenvectors of the covariance matrix and the eigenvalues quantify the variance along these directions. Hence, the lengths of the axes of the ellipse representing one standard deviation correspond to the square roots of the eigenvalues of the original covariance matrix. With this notion, Equation 4 simplifies Equation 2 such that d is lumped with the covariance matrix. As a result, the lengths of the ellipse axes (a and b) are computed for any Mahalanobis distance with Equation 5, where $\lambda(\cdot)$ is the eigenvalue function.

$$(\boldsymbol{X}-\boldsymbol{\mu})^T(d^2\boldsymbol{\Sigma})^{-1}(\boldsymbol{X}-\boldsymbol{\mu})=1 \quad (4) \qquad \begin{bmatrix} a \\ b \end{bmatrix} = \sqrt{\lambda(d^2\boldsymbol{\Sigma})} = d\sqrt{\lambda(\boldsymbol{\Sigma})} = d\sqrt{\boldsymbol{\lambda}} \quad (5)$$

The relationship illustrated in Equation 5 linking elliptical geometry parameters (a and b), the Mahalanobis distance (d) for a specified confidence level, and the covariance matrix in terms of eigenvalues ($\boldsymbol{\lambda}$) enables the development of a method for adjusting ellipse dimensions. Given an initial rectangular OVB and a confidence level of M%, the goal is to determine the ellipse representing the N% confidence level through the following steps:

1) Compute the initial lengths of the ellipse axes (a_0, b_0) based on the length and width of the rectangular OVB, respectively.
2) Calculate the Mahalanobis distance of the initial ellipse, denoted as $d_0 = \sqrt{(\chi_2^2)^{-1}(M/100)}$.
3) Determine the Mahalanobis distance for the desired ellipse, given by $d = \sqrt{(\chi_2^2)^{-1}(N/100)}$.
4) Compute the new lengths of the ellipse axes (a, b) using the relationship in Equation 6. It leverages the fact that the eigenvalues in both ellipses are the same.

$$\begin{bmatrix} a \\ b \end{bmatrix} = \frac{d}{d_0} \begin{bmatrix} a_0 \\ b_0 \end{bmatrix} \quad (6)$$

As can be seen, transforming a given ellipse from one level of confidence to another boils down to the multiplication of the initial ellipse dimensions by the ratio of their Mahalanobis distances. The ability of manipulating confidence ellipses enables any SD approach to deconflict OVBs with a buffer proportional to the original OVB dimensions. This buffer is created by inflating the original encapsulated ellipses based on a desired, more conservative confidence level.

B. Ellipse-based strategic deconfliction

To assess the impact of inflating confidence ellipses, the chosen strategic deconfliction approach is the single depot "Rolling Horizon with K-Position Search" [11] developed at NASA Ames. The strategic deconfliction problem is posed with a Mixed Integer Linear Programming (MILP) formulation with the goal of minimizing the average ground delay of all the UAS in a scenario while constraining the temporal separation at the depots (points of departure) and the separation at the crossing waypoints between flights traveling different trajectories, such that there is no overlap between their OVBs. Instead of deconflicting all the planned flights at once, the approach solves the MILP problem for a pre-defined rolling time horizon for each order permutation of the first k flights. The permutation with the lowest ground delay is selected, the first flight departure time is fixed and the optimization problem is repeated by shifting the rolling horizon forward one flight in the departure queue. The deconfliction is terminated once the algorithm has traversed the complete queue of departing flights. Given the on-demand nature of the delivery requests and the required flight preparation time, ground delay can only be positive; departure before the delivery request is not possible.

In this study, only the geometrical constraints that define the temporal separation at the crossing waypoints have to be modified (see Equations 11 and 12 in [11]) to accommodate elliptical OVS instead of the standard rectangular version. To that end, the overlapping elliptical OVSs of the trajectories that conform the crossing waypoint are identified, followed by their projection onto the temporal line to compute the minimum temporal separation. As can be observed in Figure 2, finding the overlapping ellipses consists of first filtering the pool of potential intersecting ellipses into two smaller sets — A and B, one for each vehicle — and then checking for overlap for every pair combination ($\forall A \times B$).

Finding the overlapping ellipses by checking each pair between both paths is computationally expensive. Instead, a heuristic is adopted in step 1 of Figure 2 to discard most pairs and focus only on those with the highest potential of overlap. Figure 3 illustrates this approach, where the vehicles in paths A and B are called the ownship and the intruder, respectively. The goal is to only compare the red ellipses of the intruder that either intersect or are contained within the tangential lines drawn from the ownship's ellipses along its flight path direction (set B), with the red ellipses of the ownship that similarly intersect or are contained within the tangential lines drawn from the intruder's ellipses (set A).

The first intruder ellipse of set B (B_1) is centered right before or after the intersection of the intruder's flight path and the ownship's line closest to the intruder's depot ($\mathbf{I_{o_1}}$), as can be seen in Figure 4. To determine B_1, an arbitrary point along the ownship's line ($\mathbf{Q_{o_1}}$) is selected and connected to each intruder ellipse center progressively from the depot to the destination. When the angle between the vector representing the direction of the ownship line and the vector from the arbitrary point to the ellipse center changes sign, the two ellipse centers that qualify as potential B_1 candidates have been identified. Subsequently, it is verified whether the ellipse of the candidate pair closest to the intruder's depot

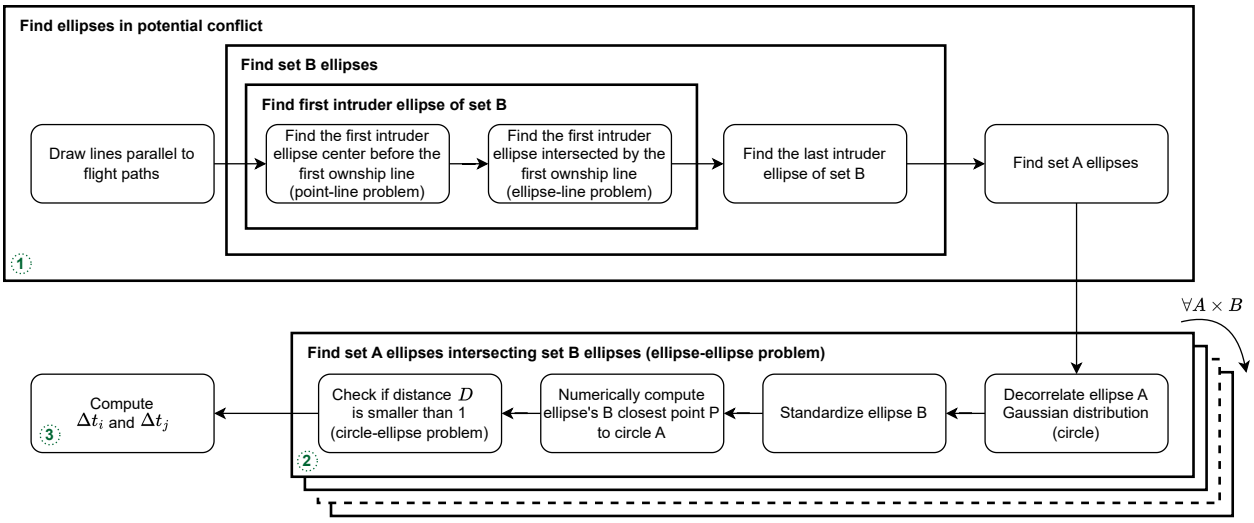

Fig. 2 Temporal separation 3-step computation for the ellipse-based strategic deconfliction approach.

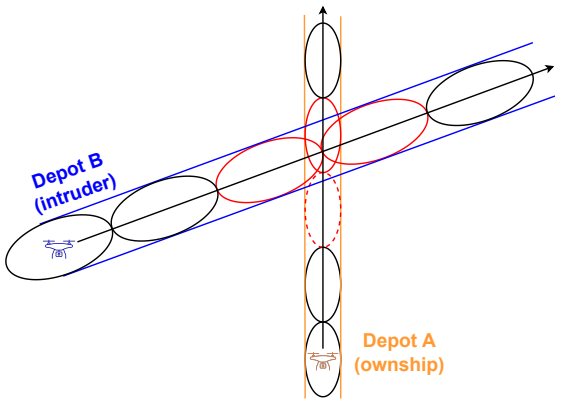

Fig. 3 Crossing waypoint example.

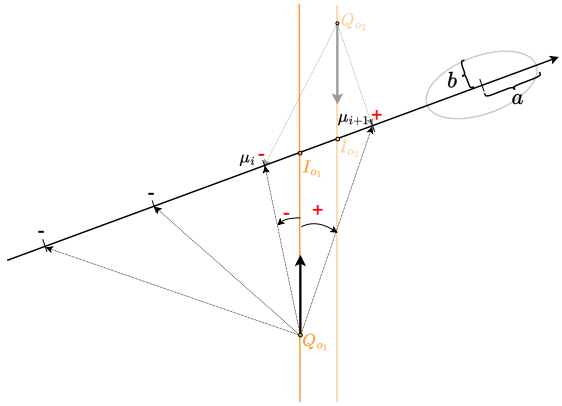

Fig. 4 Identification of set B's first and last ellipses.

intersects with the ownship's line using Equation 7; where $\boldsymbol{\mu_i}$ is the center of the ellipse, a and b are the semi-axes lengths, and ϕ_i and ϕ_o are the azimuths of the intruder's and ownship's flight paths, respectively. The derivation of this inequality can be found in the Appendix. If this condition is satisfied, then this ellipse becomes the initial member of set B; otherwise, the second candidate assumes this role.

$$\left(\|\mathbf{Q_{o_1}} - \boldsymbol{\mu_i}\| \sin\left(\phi_o - \angle(\mathbf{Q_{o_1}} - \boldsymbol{\mu_i})\right)\right)^2 < (a \sin(\phi_o - \phi_i))^2 + (b \cos(\phi_o - \phi_i))^2 \tag{7}$$

Once B_1 is found, the same iterative process is repeated to discover the last ellipse of set B using the second ownship line and a new arbitrary point on this line ($\mathbf{Q_{o_2}}$). However, instead of starting from the depot, B_1 is the first candidate. The iterative process halts when the pair of ellipses that define a change in angle sign has been found. The last ellipse of set B corresponds to the last candidate that intersects the second ownship line according to Equation 7. Exactly the same process is repeated to find the ownship ellipses that make up set A.

As can be observed for the red dashed ellipse in Figure 3, being part of set A or B does not guarantee an ellipse intersection. Hence, step 2 in Figure 2 is to check for each pair, one ellipse of set A and another from set B, whether they intersect. For that purpose, the ellipse to ellipse intersection problem is simplified. The ellipse of set A is first decorrelated with $\boldsymbol{L}$, the lower triangular matrix of the Cholesky decomposition of its correlation matrix $\boldsymbol{\Sigma_A} = \boldsymbol{L}\boldsymbol{L}^T$. Then, the ellipse from set B is standardized using the rotation matrix defined in Equation 8, where the rotation angle τ is defined as the negative of the angle corresponding to the eigenvector associated with the highest eigenvalue of the transformed matrix $\boldsymbol{L}^{-1}\boldsymbol{\Sigma_B}(\boldsymbol{L}^{-1})^T$. Figure 5 shows the resulting geometry: a circle with center in $\boldsymbol{\mu_{A_T}} = -\boldsymbol{R}\boldsymbol{L}^{-1}(\boldsymbol{\mu_B} - \boldsymbol{\mu_A})$ and an ellipse centered at the origin with correlation matrix $\boldsymbol{\Sigma_{B_T}} = \boldsymbol{R}\boldsymbol{L}^{-1}\boldsymbol{\Sigma_B}(\boldsymbol{L}^{-1})^T\boldsymbol{R}^T$.

$$\boldsymbol{R} = \begin{bmatrix} \cos\tau & -\sin\tau \\ \sin\tau & \cos\tau \end{bmatrix} \tag{8}$$

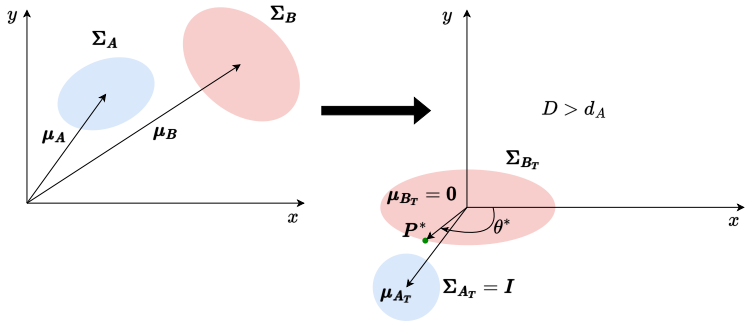

Fig. 5 Geometrical simplification of ellipse pair intersection.

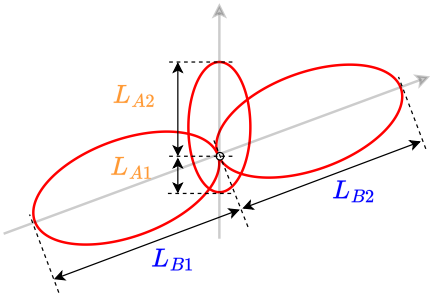

Fig. 6 Temporal separation distances.

The final ellipse and circle are intersecting if the shortest distance between them D (Equation 9) is smaller than the circle radius, which coincides with the Mahalanobis distance d_A of set A's original elliptical distribution confidence level ($D < d_A$). If the ellipse defined by (μ_A, Σ_A) represents a confidence region of 95%, $d_A = \sqrt{(\chi^2_2)^{-1}(95/100)} = 2.45$. Equation 10 embodies the coordinates of the closest point $\boldsymbol{P^*}$ in the ellipse to the circle, where θ^* is the angle described by the vector $\overrightarrow{\boldsymbol{\mu_{B_T}P}}$. Unfortunately, there does not exist an analytical expression for θ^*, so it is computed numerically using the gradient descent method. Equation 11 provides the step update, where γ is the learning rate that controls the update step size; Equation 12 describes a reasonable initial guess that connects the centers of the ellipse and the circle; and Equation 13 and Equation 14 provide the first derivatives of the squared distance and the location of $\boldsymbol{P}$ with respect to the angle θ, respectively. To prevent the parameters θ from straying too far from θ_0, which is near θ^*, γ is initialized to a constant value of 0.05, normalized with the maximum distance from the center of the circle to the endpoints of the ellipse's axes. Furthermore, γ is scheduled to be halved every 20 iterations. The optimization concludes when the update error is less than 10^{-7} or the maximum of 1000 iterations has been reached.

$$D^2 = (\boldsymbol{P} - \boldsymbol{\mu_{A_T}}) \cdot (\boldsymbol{P} - \boldsymbol{\mu_{A_T}}) \tag{9}$$

$$\boldsymbol{P^*} = \begin{bmatrix} a\cos\theta^* \\ b\sin\theta^* \end{bmatrix} \tag{10}$$

$$\theta_{t+1} = \theta_t - \gamma \frac{dD^2}{d\theta} \tag{11}$$

$$\theta_0 = \tan^{-1}\left(\frac{a}{b}\frac{\mu_{A_{T_y}}}{\mu_{A_{T_x}}}\right) \tag{12}$$

$$\frac{dD^2}{d\theta} = 2\frac{d\boldsymbol{P}}{d\theta} \cdot (\boldsymbol{P} - \boldsymbol{\mu_{A_T}}) \tag{13}$$

$$\frac{d\boldsymbol{P}}{d\theta} = \begin{bmatrix} -a\sin\theta \\ b\cos\theta \end{bmatrix} \tag{14}$$

After having found the intersecting ellipses, step 3 of Figure 2 consists of finding the temporal separation to prevent conflict at the intersections. Since the temporal separation depends on which UAS sequences the crossing waypoint first, Equation 15 and Equation 16 are the two new constraints that substitute those in the original strategic deconfliction MILP formulation. Here, Scheduled Time of Arrival or $STA(\cdot)$ stands for the time at which the $(\cdot)$ UAS is scheduled to sequence the crossing waypoint; M is the Big-M value required for linearisation [11]; $\omega(A, B)$ is the decision variable defined in Equation 17; $L_{\_1}$ and $L_{\_2}$ are the distances of the overlapping ellipses of depot $(\_)$ before and after the path intersection, as can be seen from the example geometry in Figure 6; and V_{cA} and V_{cB} are the cruise ground speed for the vehicles departing from depots A and B, respectively.

$$(STA(B) - STA(A)) + M(1 - \omega(A,B)) \geq \Delta t_A, \quad \text{where } \Delta t_A = \frac{L_{A2}}{V_{cA}} + \frac{L_{B1}}{V_{cB}} \tag{15}$$

$$(STA(A) - STA(B)) + M\omega(A,B) \geq \Delta t_B, \quad \text{where } \Delta t_B = \frac{L_{A1}}{V_{cA}} + \frac{L_{B2}}{V_{cB}} \tag{16}$$

$$\omega(A,B) = \begin{cases} 1, & STA(A) < STA(B) \\ 0, & \text{otherwise} \end{cases} \tag{17}$$

C. Safety and efficiency metrics

1. Safety metric: Number of collisions per flight hour

This section develops a metric for quantifying the impact on safety by the confidence level that determines the ellipse's geometry. Let's denote $\mathcal{F}$ as the set of all flights planned in the scenario in chronological order of departure (Equation 18) and C as the set of unordered pairs of flights that are in the air at the same time (Equation 19, where $\text{Dep}(f_x)$ and $\text{Arr}(f_x)$ stand for the departure and arrival times of flight f_x. The number of flight pairs is $|C|$ and each of the flights is composed of n_x ellipses (e), as shown in Equation 20.

$$\mathcal{F} =: \left\{ f_i | \text{Dep}(f_i) \leq \text{Dep}(f_{i+1}),\ \forall i = 1, 2, \ldots, n_f \right\} \tag{18}$$

$$C =: \left\{ (f_\alpha, f_\beta) | f_\alpha, f_\beta \in \mathcal{F};\ \alpha < \beta;\ \text{Dep}(f_\alpha) < \text{Dep}(f_\beta) < \text{Arr}(f_\alpha) \right\} \tag{19}$$

$$\begin{aligned} f_\alpha &= \left(e_{\alpha 1}, e_{\alpha 2}, \ldots, e_{\alpha n_\alpha} \right) \\ f_\beta &= \left(e_{\beta 1}, e_{\beta 2}, \ldots, e_{\beta n_\beta} \right) \end{aligned} \tag{20}$$

The probability of collision between an ellipse i of flight α ($e_{\alpha i}$) with another of flight β ($e_{\beta j}$) that completely overlap in time (start and end at the same points in time) is computed using Hwang's method described in [12], a numerical approach that first approximates the elliptical confidence region as a rectangle and then trims its corners for a more accurate estimation. However, that perfect time overlapping may not be true in practice. Hence, a time weighted average is taken in Equation 21 to compute the probability of collision between an ellipse i of flight α with the complete flight β. $P_{\alpha i,\beta j}$ is Hwang's probability of collision between ellipses $e_{\alpha i}$ and $e_{\beta j}$. $\xi_{\alpha i,\beta j}$ are the average weights defined in Equation 22, which quantify the percentage of time of the α flight i^{th} ellipse during which the β flight j^{th} ellipse is also active. $t_{0_{xy}}$ and $t_{f_{xy}}$ are the start and end times of ellipse y within flight x, respectively.

$$P_{\alpha i,\beta} = \sum_{j=1}^{n_\beta} \xi_{\alpha i,\beta j} \cdot P_{\alpha i,\beta j} \tag{21}$$

$$\xi_{\alpha i,\beta j} = \begin{cases} 0, & (t_{0_{\alpha i}} \geq t_{f_{\beta j}}) \vee (t_{f_{\alpha i}} \leq t_{0_{\beta j}}) \\ 1, & (t_{0_{\beta j}} \leq t_{0_{\alpha i}} < t_{f_{\beta j}}) \wedge (t_{0_{\beta j}} < t_{f_{\alpha i}} \leq t_{f_{\beta j}}) \\ \dfrac{t_{f_{\alpha i}} - t_{0_{\beta j}}}{t_{f_{\alpha i}} - t_{0_{\alpha i}}}, & (t_{0_{\beta j}} < t_{f_{\alpha i}} \leq t_{f_{\beta j}}) \wedge (t_{0_{\beta j}} > t_{0_{\alpha i}}) \\ \dfrac{t_{f_{\beta j}} - t_{0_{\alpha i}}}{t_{f_{\alpha i}} - t_{0_{\alpha i}}}, & (t_{0_{\beta j}} \leq t_{0_{\alpha i}} < t_{f_{\beta j}}) \wedge (t_{f_{\beta j}} < t_{f_{\alpha i}}) \\ \dfrac{t_{f_{\beta j}} - t_{0_{\beta j}}}{t_{f_{\alpha i}} - t_{0_{\alpha i}}}, & (t_{f_{\beta j}} \leq t_{f_{\alpha i}}) \wedge (t_{0_{\beta j}} \geq t_{0_{\alpha i}}) \end{cases} \tag{22}$$

Given the probability of collision between one ellipse and a complete flight, Equation 23 computes the number of near mid-air collisions between two flights ($\text{NMAC}_{\alpha,\beta}$) and Equation 24 calculates the number of near mid-air collisions between all flight combinations in the scenario (NMAC_C). In order to translate the probability into the number of near mid-air collisions (deterministic), it is multiplied by $N_{\alpha i}$ — the number of times that the probability distribution represented by the confidence ellipse is sampled. Equation 25 shows that $N_{\alpha i}$ is proportional to the duration

of the ellipse divided by the chosen elapsed time between samples T (e.g. 5 min, 1 min, 1 second, etc.). The existence of the T hyper-parameter does not allow the comparison of the results with existing Target Levels of Safety (TLS). However, it enables a relative safety comparison between scenarios with ellipses of different degrees of confidence. The authors do not discard the possibility that TLS could be defined in the future for specific values of T in order to facilitate the certification of safety studies with probabilistic operational intent. Finally, to obtain the Level of Safety (LS) of a scenario, Equation 26 divides the total number of near mid-air collisions in a scenario by the total number of flight hours flown between all the flights.

$$\mathrm{NMAC}_{\alpha,\beta} = \sum_{i=1}^{n_\alpha} P_{\alpha i,\beta} \cdot N_{\alpha i} \tag{23}$$

$$\mathrm{NMAC}_{C} = \sum_{(f_\alpha, f_\beta) \in C} \mathrm{NMAC}_{\alpha,\beta} \tag{24}$$

$$N_{\alpha i} = \frac{t_{f_{\alpha i}} - t_{0_{\alpha i}}}{T} \tag{25}$$

$$\mathrm{LS} = \frac{\mathrm{NMAC}_{C}}{\sum_{f \in \mathcal{F}} \mathrm{Arr}(f) - \mathrm{Dep}(f)} \tag{26}$$

The outlined step-by-step computation of the safety metric can be observed in Figure 7. Among its benefits, it does not require that flights start simultaneously, ellipse's of different flights start and end simultaneously, same ellipse duration between different flights or same ellipse duration between the ellipses of the same flight.

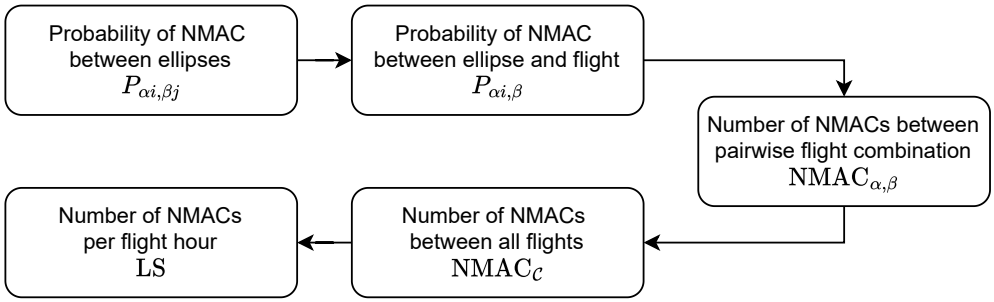

Fig. 7 Safety metric step-by-step computation.

2. Efficiency metric: Ground delay

The chosen metric for assessing the efficiency of the strategic deconfliction approach given the rectangles or ellipsoids representing a certain degree of confidence level is ground delay [2]. Equation 27 computes the scenario ground delay, where $\mathrm{Req}(f)$ is the earliest time at which the vehicle could take-off after a package delivery was requested for flight f and $\mathrm{Dep}(f)$ is its actual departure time.

$$\mathrm{GD} = \frac{1}{n_f} \sum_{f \in \mathcal{F}} (\mathrm{Dep}(f) - \mathrm{Req}(f)) \tag{27}$$

D. Route network structures

Four route network structures simulated in the San Francisco Metropolitan Area were considered for the present research with increasing degrees of complexity. Considering the same two depots and starting with one route per depot, a new route is added to each depot crossing all opposing depot routes and increasing the delivery demand at each depot by a constant factor. Figure 8 illustrates the most complex route network structure where all considered routes are active. The other route network structures are subsets where only 1, 2 or 3 of those routes are activated for each depot. As a result, the number of crossing waypoints in each scenario is r^2 — where r is the number of routes that originate at each depot — and the traffic density is σr — where σ is the traffic density per route, which is constant between all route network structures. As in previous works [2, 11], the on-demand service request to deliver a package from a depot to a drop-off location is simulated using a Poisson distribution with its rate parameter, in this case, equal to twice the time that the UAS traverses an OVB or OVS (departure spacing).

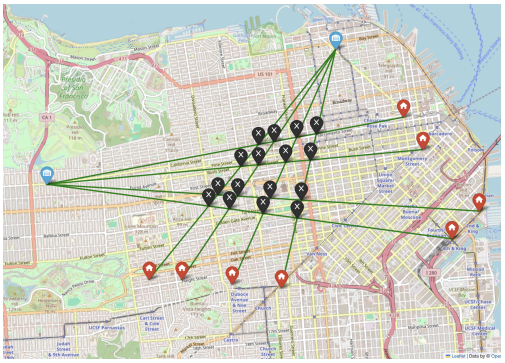

Fig. 8 Most complex route network structure for UTM scenario simulation in San Francisco Metropolitan Area [11].

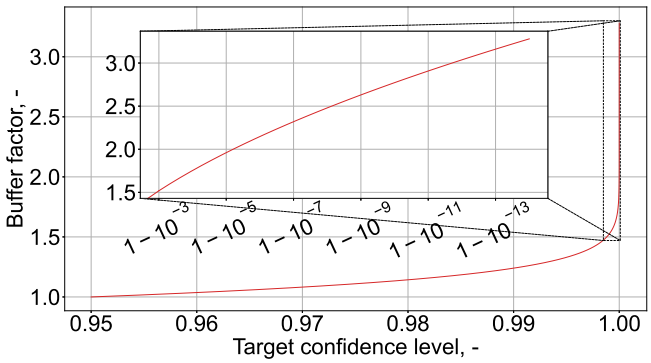

Fig. 9 Buffer expansion factor with respect to the target level of confidence.

IV. Results

The impact of a separation buffer was evaluated on the single depot K-position strategic deconfliction approach with ellipses proposed in Section III.B in terms of the safety and efficiency metrics discussed in Section III.C for the four different degrees of route network complexity presented in Section III.D. The buffer was created by increasing the desired OVS level of confidence, as explained in Section III.A, to fifteen different levels: 10 between 95% and 99.5% in steps of 0.5%, and 5 from the set $\{100 - 10^{-n} \mid n \in \mathbb{N}\}$%. Additionally, the results were compared to the baseline with rectangles, where the buffer was created by expanding the inscribed ellipses in the original OVBs as in Section III.A and deconflicting the rectangles circumscribing the expanded ellipses following the temporal separation from [2]. In contrast with previous research, non-overlapping OVSs or OVBs do not guarantee 100% safety.

For each number of routes, buffer level of confidence and geometrical shape of the distribution (elliptical or rectangular), 100 scenarios were run in order to remove the effects of the variability introduced by the Poisson distribution and the selected routes when the scenario had less than 4. Table 1 shows the values of all the parameters in the K-Position strategic deconfliction approach that were kept constant in all the scenarios. As can be seen, every vehicle went through seven flight phases, namely vertical take-off, climb, transition to cruise (acceleration), cruise, transition from cruise (deceleration), descent and vertical landing. Only during the cruise phase, OVSs or OVBs are generated for deconfliction and the computation of the safety metric. The loss of separation radius was used as threshold for declaring an NMAC. The scenario concludes when all the vehicles have reached their drop-off locations.

Table 1 K-Position Search [11] parameters

Parameter	Values	Parameter	Values
Number of flights per route	10 [-]	Loss of separation radius	42.5 [m] [4]
Poisson demand rate	60^{-1} [s^{-1}]	Original confidence level	95%
Rolling horizon window	300 [s]	Vertical take-off and landing time	15 [s]
Local neighborhood search (k)	2 [-]	Climb distance and time	600 [m] and 61 [s]
Flight preparation time	3600 [s]	Transition distance and time	50 [m] and 3.35 [s]
Minimum separation time	30 [s]	Cruise airspeed	20 [m/s]
OVS/OVB length and width	600 [m] and 200 [m]	Descent distance and time	600 [m] and 59 [s]

A. Buffer factor

Figure 9 shows the buffer factor ($\frac{d}{d_0}$) as a function of the expansion target level of confidence (N) given an original confidence level (M) of 95%. Notably, the original OVS dimensions increase by a factor of 1.5 when the confidence level rises from 95% to around 99.9% ($\Delta = 4.9\%$). This increase is followed by a further growth of 1.75 times when the confidence level is elevated from 99.9% to ≈100% ($\Delta < 0.1\%$). Interestingly, in this final 0.1% range, the buffer expands more significantly than during the initial 4.9% increase.

B. Safety

The left plot of Figure 10 illustrates safety outcomes as measured by the metric discussed in Section III.C.1 using a probability sampling rate (T) of 1 Hz. As expected, the absence of an SD poses the highest risk, reflected in the largest number of NMAC per flight hour. Conversely, the SD with rectangles yields the best safety performance due to its method of computing the temporal separation between the OVBs of different depots at crossing points. As noted in [11], this approach relies on an approximation that results in a conservative estimate of temporal separation, inadvertently creating an additional variable buffer. In contrast, the SD with ellipses presented in Section III.B allows for OVSs to be tangential to one another, thereby increasing the risk of collisions. Furthermore, in both SD types it can be observed that the increased complexity in the route network structure leads to a higher number of NMAC per flight hour, degrading the safety. Similarly to the buffer factor discussed in Section IV.A, most of the safety benefit is gained in the last 0.1% of the target confidence level.

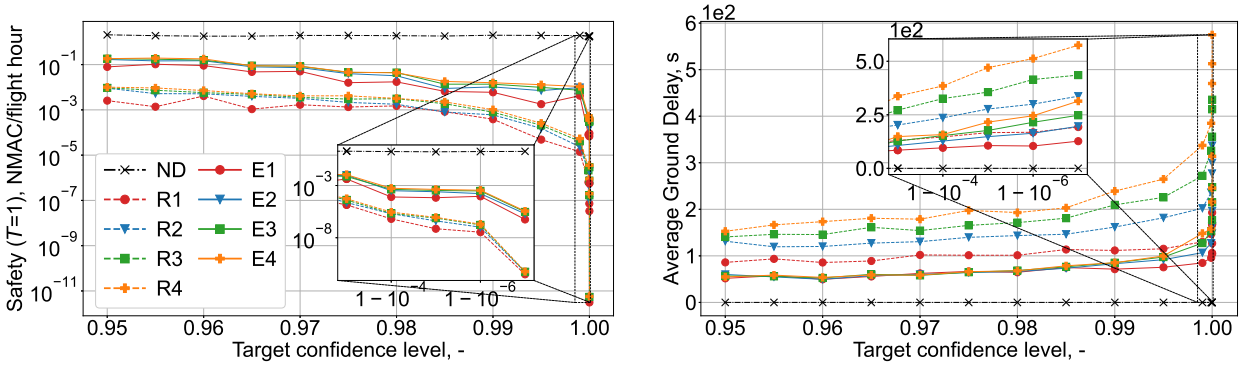

Fig. 10 Evaluation metrics for different targets of confidence level and route network complexity. The dotted-dashed black line reflects the safety when there is no deconfliction (ND), whereas the solid and dashed lines represent the SD with ellipses (E) and rectangles (R), respectively. The number for the solid and dashed lines represents the number of routes. [Left] Safety metric as the number of NMAC per flight hour with a probability sampling rate (T) of 1 Hz. [Right] Efficiency metric as the average ground delay per flight in seconds.

Figure 11 illustrates the temporal separation between vehicles at the crossing point of the single-route network structure, highlighting the aforementioned differences in buffer size. The rectangle-based SD exhibits an additional average temporal separation of 30 second compared to its ellipse-based counterpart at a confidence level of 95%, and it doubles to 60 seconds at ≈100%. The faster increase in temporal separation of the rectangle-based SD explains its accelerated decline in the number of NMAC per flight hour shown in Figure 10. This trend is specially notorious for the last plotted values of the target confidence level, where the temporal separation approaches the average cruise flight duration of 240 seconds. For the shortest flights, this duration decreases to 180 seconds, further reducing the overlap in airborne time between vehicles from different depots.

Furthermore, the comparison of the single scenario curves in Figure 11 reveals distinct behaviors between the two approaches: the rectangle-based SD increases smoothly with buffer size, whereas the temporal separation of the ellipse-based method remains constant, only increasing at specific target confidence levels. The methodology discussed in Section III.B shows that, despite an increase in buffer size, the temporal separation for the elliptical version only grows when new ellipses from different depots overlap.

Finally, the impact of the larger buffer and temporal separation can be observed on the maximum number of potential encounters in a scenario, as illustrated in Figure 12. The number of potential encounters at a scenario time step is defined in this research as the product of the numbers of airborne vehicles from both depots. It can be observed that the difference in the maximum number of potential encounters between the two approaches widens as the target level of confidence rises, with an increase of nearly threefold from the first to the last data point.

C. Efficiency

The average ground delay per flight is the metric used to evaluate efficiency, as illustrated in the right plot of Figure 10. As expected, when there is no SD, the vehicles depart when requested after the preparation time with no delays. Vehicles in the rectangle-based SD suffer a greater delay than the ellipse-based counterpart due to the additional

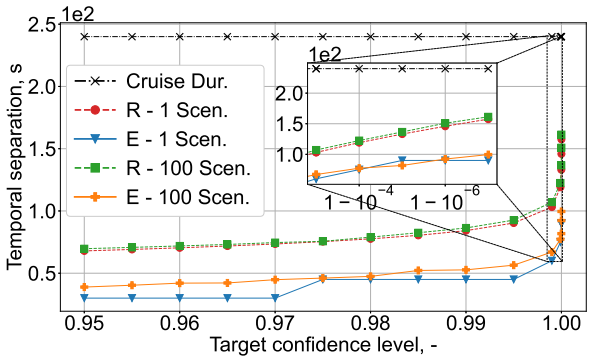

Fig. 11 Temporal separation between vehicles at the crossing point of the single route network structure for SD with ellipses (E) and rectangles (R) as a function of the target confidence level. It shows 1 scenario and averaged over 100 scenarios. The dotted-dashed line reflects the average cruise flight duration.

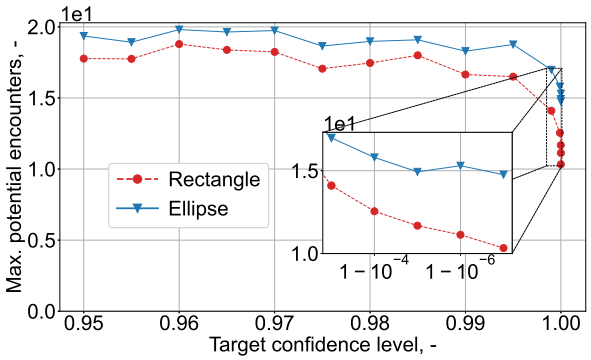

Fig. 12 Maximum number of potential encounters as a function of the target confidence level for the single route network structure for the SD with rectangles (dashed) and ellipses (solid).

buffer discussed in Section IV.B. Additionally, the greater the route network complexity, the greater their average ground delay and the greater its rate of growth. The ellipse-based approach presents the same delay independently of complexity up to a 99% target confidence level, when it starts to exhibit the same behavior as with the rectangular geometry.

D. Computation time

The method proposed in literature [11] exploits an analytical geometrical approximation for the computation of the temporal separation. In contrast, the methodology presented here computes the temporal separation by finding the overlapping ellipses through numerical computation after having discarded most of the non-overlapping candidates using the heuristics discussed in Section III.B. Besides safety and efficiency, computation time also has to be assessed when considering the deployment of the proposed algorithm in real-time applications.

In Figure 13, it can be seen that the computation time remains constant for the rectangle-based SD, whereas it increases with the target confidence level for the ellipse-based counterpart. As the inflated ellipses grow with the buffer, they potentially intersect more ellipses from the opposing depot. This increases the size of sets A and B from Figure 2, leading to a larger number of "ellipse-ellipse problems" that have to be resolved numerically. As a result, the SD with ellipses is 3 times (at 95%) to 8 times (at ≈100%) more computationally expensive than the rectangle-based version.

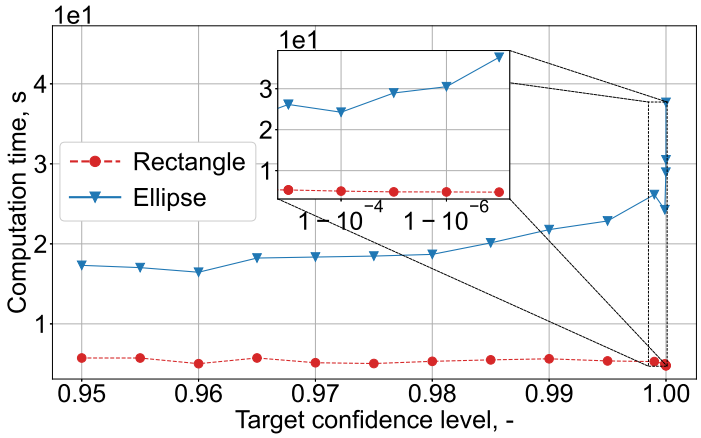

Fig. 13 Computation time versus target confidence level for the SD with rectangles (dashed) and ellipses (solid).

V. Conclusion

This paper proposes a methodology for creating an Operational Volume Block (OVB) buffer for deconfliction as a function of the initial dimensions of the elliptical Operational Volume Segment (OVS) inscribed in the OVB. According to ASTM standards, OVBs are constructed such that the vehicle's position is inside of the OVB for 95% (original confidence level) of the time. Now a buffer can be created by inflating the OVS to a more conservative target level of confidence, such as 99%. In contrast with traditional distance based buffers that seek a constant separation distance between OVBs, the proposed approach is a function of OVB dimensions and provides any deconfliction approach with a sounded control variable that can be linked to safety, namely the target confidence level.

The impact of the buffer was assessed by integrating it within the Rolling Horizon with K-Position Search pre-departure strategic deconfliction (SD) approach for on-demand package delivery scenarios over the San Francisco Metropolitan Area. Four degrees of route network structure complexity were considered by increasing the number of routes and crossing points. Besides deconflicting the original rectangular OVBs with buffer, an alternative is discussed where the inflated OVSs are deconflicted. To that end, the temporal separation equations where modified to account for the elliptical geometry. In both cases, performance was evaluated in terms of safety, for which this research outlines a methodology for computing the number of Near Mid-Air Collisions (NMAC) per flight hour given the vehicles' OVSs and original confidence levels, and efficiency, in the form of the average ground delay per vehicle.

Increasing the buffer enhances safety but reduces efficiency, especially at high target confidence levels. For a 95% confidence level OVB/OVS, the largest buffer growth occurs within the final 0.1% of the target confidence level; whereas it increases by a factor of 1.5 from 95% to 99.9%, it further grows by a factor of 1.75 from 99.9% to $\approx$100%. Furthermore, increasing the route network structure complexity has shown to negatively impact both safety and efficiency.

The original rectangle-based SD exhibits a larger buffer size for the same target confidence level compared to the ellipse-based approach due to its conservative computation of temporal separation. This discrepancy grows with the target confidence level, effectively doubling across the considered range. Consequently, it yields fewer NMAC per flight hour but greater average ground delays. Although the ellipsoidal approach presents lower safety levels for the same target confidence levels, it facilitates a controlled introduction of a buffer as a function of the level of confidence. In contrast, the rectangular SD does not address the inaccuracies inherent in its geometrical approximations.

The 3×-8× difference in computation time between the analytical rectangle-based SD and the numerical ellipse-based counterpart calls for the development of an analytical ellipse-based version with lower inference time for real time applications with high frequency updates, establishing a trade-off between efficiency and computational load. Additionally, the authors recommend exploring the development of a Neural Network based function that fills the gaps left by Hwang's method in the estimation of the probability of collision between OVSs for more accurate risk prediction.

To conclude, the authors hope that the outlined methodology for the creation of the OVB buffer and the safety evaluation metric, coupled with some target level of safety (TLS), will be used in the future to define buffer dimensions for deconfliction or new confidence levels, different than the current 95%, for the generation of OVBs. In contrast with current TLSs that just specify the number of failures per flight hour, the proposed safety metric will require the addition of a probability sampling rate (e.g. T=1 [Hz]).

Appendix

Given a line (Equation 28) and an ellipse (Equation 29) in standard form, the line and the ellipse intersect when the condition in Equation 30 is met. This inequality is obtained by substituting the line equation in the ellipse equation, simplifying to the quadratic equation and then declaring the discriminant of the quadratic formula greater than zero for there to be a solution or line-ellipse intersection. a and b are the major and minor ellipse axes lengths, m is the slope of the line and c is the y-coordinate of the intersection of the line with the y-axis.

$$y = mx + c \tag{28}$$

$$\frac{x^2}{a^2} + \frac{y^2}{b^2} = 1 \tag{29}$$

$$c^2 < (am)^2 + b^2 \tag{30}$$

The problem arises when the ellipse is not in standard form. This can be solved by rotating the ellipse and the line about the ellipse center and shifting both geometries such that the ellipse center ($\boldsymbol{\mu_i}$) is at the center of coordinates, as shown in Figure 14. Then, the point where the ownship line intersects the y-axis of the transformed space (c) can be computed with Equation 31, where η is the angle between the ownship line and the intruder's ellipse major axis (Equation 32).

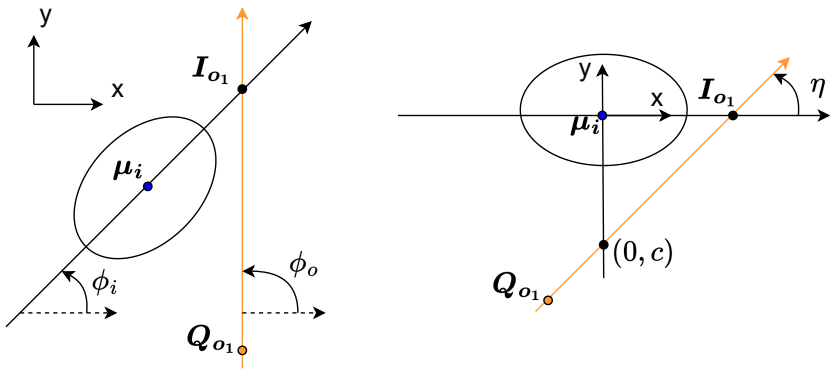

Fig. 14 Original and transformed geometry after ellipse standardization.

$$c = -\|\boldsymbol{I_{o_1}} - \boldsymbol{\mu_i}\| \tan\eta \tag{31}$$

$$\eta = \phi_o - \phi_i \tag{32}$$

The point $\boldsymbol{I_{o_1}}$ is the intersection of the ownship line and the intruder line of ellipse centers. This point can be found by equating these lines, as in Equation 33. $\boldsymbol{v_o}$ and $\boldsymbol{v_i}$ are the direction vectors of both lines, whereas $\boldsymbol{Q_{o_1}}$ is an arbitrary point on the ownship line. By solving for t_c in the x-axis equation and substituting it into the y-axis equation, $\boldsymbol{s_c}$ is found to be Equation 34.

$$\begin{aligned} \boldsymbol{I_{o_1}} &= \boldsymbol{Q_{o_1}} + t_c \boldsymbol{v_o} = \boldsymbol{\mu_i} + s_c \boldsymbol{v_i} \\ \boldsymbol{Q_{o_1}} + t_c \frac{\cos\phi_o}{\sin\phi_o} &= \boldsymbol{\mu_i} + s_c \frac{\cos\phi_i}{\sin\phi_i} \end{aligned} \tag{33}$$

$$\boldsymbol{s_c} = \frac{\sin\phi_o \left(Q_{o_{1x}} - \mu_{i_x}\right) - \cos\phi_o \left(Q_{o_{1y}} - \mu_{i_y}\right)}{\sin\eta} \tag{34}$$

Then, Equation 34 is substituted on the right side of Equation 33 and the resulting expression is fed into Equation 31. The final intersection coordinate with the transformed y-axis is reflected in Equation 35.

$$c = \left[\cos\phi_o \left(Q_{o_{1y}} - \mu_{i_y}\right) - \sin\phi_o \left(Q_{o_{1x}} - \mu_{i_x}\right)\right] \frac{\tan\eta}{\sin\eta} = \frac{\boldsymbol{v_o} \times (\boldsymbol{Q_{o_1}} - \boldsymbol{\mu_i})}{\cos\eta} = \frac{\|\boldsymbol{Q_{o_1}} - \boldsymbol{\mu_i}\| \sin\left(\phi_o - \angle\left(\boldsymbol{Q_{o_1}} - \boldsymbol{\mu_i}\right)\right)}{\cos\eta} \tag{35}$$

Finally, the simplified equation for c is incorporated into the condition specified in Equation 30. By substituting $m = \tan\eta$ and simplifying further, the final inequality is represented in Equation 36.

$$\left(\|\boldsymbol{Q_{o_1}} - \boldsymbol{\mu_i}\| \sin\left(\phi_o - \angle\left(\boldsymbol{Q_{o_1}} - \boldsymbol{\mu_i}\right)\right)\right)^2 < (a\sin\eta)^2 + (b\cos\eta)^2 \tag{36}$$

References

[1] "Standard Specification for UAS Traffic Management (UTM) UAS Service Supplier (USS) Interoperability," , 2021. URL https://www.document-center.com/standards/show/ASTM-F3548.

[2] Pradeep, P., Munishkin, A. A., Kalyanam, K. M., and Erzberger, H., "Strategic Deconfliction of Small Unmanned Aircraft Using Operational Volume Blocks at Crossing Waypoints," *AIAA SciTech 2023 Forum*, 2023. https://doi.org/10.2514/6.2023-1654.

[3] Egorov, M., Evans, A., Campbell, S., Zanlongo, S., and Young, T., "Evaluation of UTM strategic deconfliction through end-to-end simulation," *14th USA/Europe Air Traffic Management Research and Development Seminar (ATM2021)*, 2021, pp. 20–23.

[4] Evans, A. D., Egorov, M., Anand, A., Campbell, S. E., Zanlongo, S., Young, T., and Sarfaraz, N., "Safety Assessment of UTM Strategic Deconfliction," *AIAA SCITECH 2023 Forum*, 2023. https://doi.org/10.2514/6.2023-0965, URL https://arc.aiaa.org/doi/abs/10.2514/6.2023-0965.

[5] Federal Aviation Administration, "UTM concept of operations 2.0," , 2020. Accessed on 05-05-2024.

[6] Verma, S. A., Monheim, S. C., Moolchandani, K. A., Pradeep, P., Cheng, A. W., Thipphavong, D. P., Dulchinos, V. L., Arneson, H., Lauderdale, T. A., Bosson, C. S., Mueller, E. R., and Wei, B., "Lessons Learned: Using UTM Paradigm for Urban Air Mobility Operations," *2020 AIAA/IEEE 39th Digital Avionics Systems Conference (DASC)*, 2020, pp. 1–10. https://doi.org/10.1109/DASC50938.2020.9256650.

[7] Hsieh, C., Sibai, H., Taylor, H., Ni, Y., and Mitra, S., "SkyTrakx: A Toolkit for Simulation and Verification of Unmanned Air-Traffic Management Systems," *2021 IEEE International Intelligent Transportation Systems Conference (ITSC)*, 2021, pp. 372–379. https://doi.org/10.1109/ITSC48978.2021.9564492.

[8] Xue, M., Kuo, V. H., de Alvear Cardenas, J. I., and Pradeep, P., "A Method of Compliance for Achieving Target Collision Risk in UTM Operations," Tech. Rep. 20240003151, NASA Ames Research Center, February 2024.

[9] Pongsakornsathien, N., Bijjahalli, S., Gardi, A., Symons, A., Xi, Y., Sabatini, R., and Kistan, T., "A Performance-Based Airspace Model for Unmanned Aircraft Systems Traffic Management," *Aerospace*, Vol. 7, No. 11, 2020. https://doi.org/10.3390/aerospace7110154, URL https://www.mdpi.com/2226-4310/7/11/154.

[10] Xue, M., Jung, J., and Homola, J., "Intent Modeling and Conflict Probability Calculation for Operations in Upper Class E Airspace," *AIAA SciTech 2022 Forum*, 2022. https://doi.org/10.2514/6.2022-1508, URL https://arc.aiaa.org/doi/abs/10.2514/6.2022-1508.

[11] Pradeep, P., Yarramreddy, G. S., Amirsoleimani, N., Munishkin, A. A., Morris, R. A., Xue, M., Kalyanam, K. M., and Chour, K., "Rolling Horizon with K-Position Search Method for Strategic Deconfliction of Package Delivery UAS," *AIAA AVIATION FORUM AND ASCEND 2024*, 2024. https://doi.org/10.2514/6.2024-4456.

[12] Hwang, I., and Seah, C. E., "Intent-Based Probabilistic Conflict Detection for the Next Generation Air Transportation System," *Proceedings of the IEEE*, Vol. 96, No. 12, 2008, pp. 2040–2059. https://doi.org/10.1109/JPROC.2008.2006138.